

Forming Mechanism of Equilibrium and Non-equilibrium Metallurgical Phases in Dissimilar Materials: Illustrated With Aluminum/steel (Al-Fe) Joints

Shun-Li Shang (✉ sus26@psu.edu)

Pennsylvania State University

Hui Sun

Pennsylvania State University

Bo Pan

Pennsylvania State University

Yi Wang

Pennsylvania State University

Adam M. Krajewski

Pennsylvania State University

Mihaela Banu

University of Michigan

Jingjing Li

Pennsylvania State University

Zi-Kui Liu

Pennsylvania State University

Research Article

Keywords: Al-Fe intermetallic compounds, welding, additive manufacturing, density functional theory (DFT) based thermodynamics, phonon calculations, elastic constants

Posted Date: July 28th, 2021

DOI: <https://doi.org/10.21203/rs.3.rs-745143/v1>

License:  This work is licensed under a Creative Commons Attribution 4.0 International License.

[Read Full License](#)

**Forming mechanism of equilibrium and non-equilibrium metallurgical phases in
dissimilar materials: Illustrated with aluminum/steel (Al-Fe) joints**

Shun-Li Shang^{a,*}, Hui Sun^a, Bo Pan^b, Yi Wang^a, Adam M. Krajewski^a, Mihaela Banu,^c

Jingjing Li^b, Zi-Kui Liu^a

^a Department of Materials Science and Engineering, Pennsylvania State University, University
Park, PA 16802, USA

^b Department of Industrial and Manufacturing Engineering, Pennsylvania State University,
University Park, PA 16802, USA

^c Department of Mechanical Engineering, University of Michigan, Ann Arbor, MI 48109, USA

*E-mail: sus26@psu.edu

ABSTRACT:

Forming metallurgical phases has a critical impact on the performance of dissimilar materials joints. Here, we shed light on the forming mechanism of equilibrium and non-equilibrium intermetallic compounds (IMCs) in the dissimilar aluminum/steel joints with respect to processing history (e.g., the pressure- and temperature-profiles) and chemical composition, where the used knowledge of free energy and atomic diffusion in the Al-Fe system was taken from first-principles phonon calculations and data available in the literature. We found that the metastable while ductile (judged by the presently predicted elastic constants) Al_6Fe is a pressure (P) favored IMC observed in the processes involving high pressures. The MoSi_2 -type Al_2Fe is a brittle and a strong P -favored IMC observed at high pressures. The stable, brittle $\eta\text{-Al}_5\text{Fe}_2$ is the most commonly observed IMC (followed by $\theta\text{-Al}_{13}\text{Fe}_4$) in almost all processes, such as fusion/solid-state welding and additive manufacturing (AM), since $\eta\text{-Al}_5\text{Fe}_2$ is temperature-favored, possessing high thermodynamic driving force of formation and the fastest atomic diffusivity among all Al-Fe IMCs. Notably the ductile AlFe_3 , the less ductile AlFe , and most of the other IMCs can be formed during AM, making AM a superior process to achieve desired IMCs in dissimilar materials. In addition, the unknown configurations of Al_2Fe and Al_5Fe_2 were also examined by machine learning based datamining together with first-principles verifications and structure predictor. All the IMCs, which are not P -favored, can be identified using the conventional equilibrium phase diagram and the Scheil-Gulliver non-equilibrium simulations.

Keywords: Al-Fe intermetallic compounds; welding; additive manufacturing; density functional theory (DFT) based thermodynamics; phonon calculations; elastic constants

1 Introduction

Joining of dissimilar materials has become increasingly important to create lightweight, high-performance, and economic structures applied in various industries, for example, automotive ¹, aerospace ^{2,3}, marine ⁴, and information technology ⁵. Specially, joining of aluminum (Al) to steel/iron (Fe) is of eminent technical interest due to the use of two essential engineering materials in the same design ^{1,6}. It is known that mechanical properties of dissimilar materials are strongly affected by the type, amount/thickness, and morphology of the metallurgical phases formed at the bonding interfaces. For example, the formation of brittle intermetallic compounds (IMCs), such as η -Al₅Fe₂ ^{7,8}, is usually detrimental to the performance of dissimilar materials joints owing to the reduction of materials' strength, ductility, and fracture toughness. A great deal of efforts in chemistry and process design is hence required to avoid or reduce their formation in dissimilar materials, demanding fundamental understanding of phase stability of IMCs during various processes, for example, different pressure (P) and temperature (T) profiles under a given chemical composition.

Relevant to the present focus of Al-Fe joints, there are six IMCs shown in the equilibrium Al-Fe phase diagram under external pressure $P = 0$ GPa; see **Figure 1** which was modelled by the CALPHAD (calculations of phase diagram) approach by Sundman et al. ⁹. It includes the stable IMCs of θ -Al₁₃Fe₄, η -Al₅Fe₂, Al₂Fe, AlFe (in B2 structure), AlFe₃ (D0₃), and the metastable ϵ -Al₈Fe₅ (D8₂). In addition, the other metastable IMCs include Al₆Fe and Al_mFe ($4 \leq m \leq 4.4$) ¹⁰, which are absent in **Figure 1**. It is believed that the Al-rich IMCs (Al₁₃Fe₄, Al₅Fe₂, and Al₂Fe) are brittle and favor crack nucleation in the joints, while the Fe-rich IMCs (i.e., the BCC based AlFe and AlFe₃) show higher ductility and strength ^{7,8}. The ductility and brittleness of these IMCs are

shown in **Figure 2** according to Pugh's criterion ^{11,12}, i.e., the ratio of bulk modulus versus shear modulus (B/G) based on the present first-principles calculations (*cf.*, Sec. 2.3). It indicates the ductile Al_6Fe , Al_5Fe_8 , and AlFe_3 ; the less ductile $\text{Al}_{13}\text{Fe}_4$ and AlFe ; and the brittle Al_5Fe_2 and Al_2Fe . **Table 1** summarizes the Al-Fe IMCs formed in different processes reported in the literature. The metastable, ductile Al_6Fe was observed in the processes of direct chill casting (example #1 shown in **Table 1**) ¹⁰, high-pressure die casting (#2) ¹³, equal channel angular extrusion (#3) ¹⁴, tungsten inert gas (TIG) welding-brazing (#4) ¹⁵, and additive manufacturing (AM) via the laser powder bed fusion (#5) ¹⁶. These observations suggest that Al_6Fe is an IMC existed at high pressures. **Table 1** further depicts that most of the stable and even metastable Al-Fe IMCs were observed in the AM processes. For example, the Al_6Fe , $\text{Al}_{13}\text{Fe}_4$, Al_2Fe , Al_5Fe_2 , AlFe , and/or AlFe_3 were formed during the processes of laser powder bed fusion ¹⁶, laser cladding ¹⁷, direct energy deposition ¹⁸, laser metal deposition ¹⁹, and/or wire-arc AM ^{20,21} (see examples #5 to #10 in **Table 1**). In particular, the ductile (or less brittle) $\text{Al}_{13}\text{Fe}_4$, AlFe , and AlFe_3 ²⁰⁻²² (examples #9 to #11) were observed in the Al-Fe based functional gradient materials fabricated by additive manufacturing. These experiments indicate that AM is an exceptional process to tailor compositions and in turn the desired IMCs. In the fusion and/or solid-state welding joints, Al_5Fe_2 is the most observed IMC (usually adjoined to iron/steel) followed by $\text{Al}_{13}\text{Fe}_4$ (usually adjacent to Al) processed by, for example, laser welding ²³⁻²⁵ (see examples #13 to #15 in **Table 1**), friction-type solid state welding ²⁶⁻³⁴ (#16 to #24), cold metal transfer fusion welding ³⁵ (#25), and double electrode gas metal arc welding ³⁶ (#26). The other IMCs such as Al_2Fe and AlFe_3 were also observed in welding processes depended on welding conditions (e.g., energy inputs) ⁷; see examples #14, #21, and #22 in **Table 1**. The same as those in welding processes, Al_5Fe_2 (major) and $\text{Al}_{13}\text{Fe}_4$ were also observed in immersion tests with solid Fe and liquid Al ³⁷⁻³⁹ (see examples

#27 to #29 in **Table 1**), Al-Fe diffusion couples ⁴⁰⁻⁴² (#30 to #32), high-temperature reactive sintering ⁴³ (#12), and aluminized steel ⁴⁴ (#33).

Despite considerable observations as shown in **Table 1**, the underlying mechanism regarding the formation of Al-Fe IMCs is still lacking albeit phase stability is known to be regulated by processing history involving *T*- and *P*-profiles for a given chemistry ⁴⁵. Phase diagram, as the beginning of wisdom to guide any work in materials science and engineering ⁴⁶, is the most used tool to analyze equilibrium IMCs under a given temperature and composition (usually under external pressure $P = 0$ GPa). Additionally, non-equilibrium simulations in terms of the Scheil-Gulliver model ^{47,48} can be used to analyze the forming IMCs in fast cooling processes by assuming that no diffusion takes place in the solid and that solute redistribution in the liquid is infinitely fast ⁴⁹⁻⁵¹. The Scheil simulations have been used to, for example, design optimal composition for additively manufactured functionally graded metals ^{49,50} and predict liquidus and solidus temperatures of steel ⁵¹. In addition to phase diagram, non-equilibrium IMCs can be predicted by calculating thermodynamic driving forces for the phases of interest with respect to supercooled liquid and associated solid phases; see the predicted interface phases at the Cu/solder joints by Lee et al. ⁵². Also based on thermodynamics, non-equilibrium IMCs can be tailored by partitionless solidification or by chemical partition solidification with limited atomic diffusions; for example, the non-equilibrium solidification predicted in the Al-Sm system by Zhou and Napolitano ⁵³. It should be remarked that thermodynamic knowledge in the literature is usually at the ambient pressure or external pressure $P = 0$ GPa, thus hindering the analysis of *P*-favored phases such as Al₆Fe in the present work. In addition to thermodynamics, kinetics (diffusion) is another factor to regulate nucleation, growth, and coarsening of IMCs ^{54,55}. For example, Al₅Fe₂ and Al₁₃Fe₄ were

formed due mainly to Al and/or Fe interdiffusion in some processes; see the examples #13, #17, #18, #30, #31, and #32 in **Table 1**.

The present work aims to unveil the forming mechanism of equilibrium and non-equilibrium IMCs in dissimilar aluminum to steel joints based on thermodynamic knowledge in the Al-Fe system from (1) the present first-principles and phonon calculations based on density functional theory (DFT) and (2) the CALPHAD modeling by Sundman et al.⁹; and kinetic (diffusion) knowledge reported in the literature^{40,56,57}. A special attention in the present DFT calculations is paid to the P -included Gibbs energy in addition to the variable of temperature. The challenge for the present DFT calculations is the unknown atomic configurations of (i) Al_5Fe_2 caused by the partially occupied Wyckoff sites 4b and 8f of space group $Cmcm$ ⁵⁸ and (ii) Al_2Fe caused by the disordered Al and Fe in one of the Wyckoff sites 2i of space group $P\bar{1}$ ⁵⁹. To address this challenge, we adopt the following three approaches: (1) DFT-based USPEX (Universal Structure Predictor: Evolutionary Xtallography) predictions⁶⁰, (2) DFT-based examinations of all possible configurations for a given supercell, and (3) datamining by examining all possible configurations in the literature with their formation energies predicted by machine learning. In addition to the conventional equilibrium phase diagram, the presently Scheil non-equilibrium simulations are also used to analyze the formation of Al-Fe IMCs. The present work indicates that the forming mechanism of IMCs in dissimilar Al-Fe joints (see examples in **Table 1**) can be explained well using phase diagram, Scheil simulations, thermodynamic driving forces, P - and T -included Gibbs energies, and atomic diffusion coefficients in the Al-Fe system.

2 Methodology

2.1 Atomic configurations of Al-Fe IMCs

Most of the Al-Fe IMCs together with the constituent elements of FCC Al and BCC Fe are ordered structures. Their structures can be found in such as the Materials Project (MP) database ⁶¹ and the Open Quantum Materials Database (OQMD) ⁶²; see the Supplementary **Table S 1**. However, Al₅Fe₂ is an IMC with vacancies (Va) in its Wyckoff sites for Al atoms ⁵⁸. The structure of Al₅Fe₂ can be depicted by the following sublattice model according to its Wyckoff sites 4c, 8g, 4b (occupation of 0.32 by Al), and 8f (occupation of 0.24 by Al) of space group *Cmcm* ⁵⁸, respectively,

$$(\text{Fe})_4^c(\text{Al})_8^g(\text{Al, Va})_4^b(\text{Al, Va})_8^f \quad \text{Eq. 1}$$

For another IMC of Al₂Fe, Chumak et al. ⁵⁹ indicated that it belongs to space group $P\bar{1}$ with one of its Wyckoff sites 2i mixed with Fe (occupation of 0.705) and Al (occupation of 0.295),

$$(\text{Fe})_{10}(\text{Al})_{24}(\text{Al, Fe})_4^i \quad \text{Eq. 2}$$

Atomic configurations of Al₅Fe₂ were determined as follows in the present work. First, all the independent Al₅Fe₂ configurations were generated by the ATAT code ⁶³ using a 24-atom supercell, see Eq. 1. Second, we performed DFT calculations for the 14- to 16-atom configurations with one or two Al atoms in the Wyckoff sites 4b and 8f, respectively. For the composition of Al₅Fe₂, we also used the universal structure predictor — USPEX ^{60,64} — to predict the lowest energy configuration in terms of a 14-atom supercell; where the computational engine of USPEX is the DFT-based calculations (see also Sec. 2.3). In addition, we also included the low energy configurations of Al₅Fe₂ suggested by Vinokur et al. ⁶⁵.

Atomic configurations of Al₂Fe were also examined by the ATAT code ⁶³ based on the mixing of Al and Fe in Wyckoff site 2i (see Eq. 2) by using the 38- and 57-atom supercells of Al₂Fe. In addition, the suggested MoSi₂-type configuration by Tobita et al. ⁶⁶ was included in the present work. Aiming to search for the possible configurations of Al₂Fe, we also adopted a datamining approach by considering all the AB₂-type configurations (~ 1.3 million) in the Materials Project (MP) database ⁶¹, the Open Quantum Materials Database (OQMD) ⁶², the Crystallography Open Database (COD) ^{67,68}, and the Joint Automated Repository for Various Integrated Simulations (JARVIS) database ⁶⁹. The enthalpies of formation (ΔH_0) of these AB₂-type configurations were predicted by machine learning (ML) in terms of the tool of SIPFENN (structure-informed prediction of formation energy using neural networks) ⁷⁰. Here, SIPFENN requires only atomic configurations and atomic species, which allows efficient integration into datamining study within minutes. On a random 5% subset in the OQMD structures, SIPFENN could achieve a mean absolute error of 28 meV/atom (2.7 kJ/mol-atom) to predict ΔH_0 ⁷⁰. For the SIPFENN suggested A₂B-type configurations with lower ΔH_0 values (more than 500 configurations were selected herein), we performed DFT-based verifications. Notably, the present datamining approach found that the lowest energy configuration of Al₂Fe is also the MoSi₂-type.

2.2 First-principles thermodynamics

Thermodynamic properties at finite temperatures can be predicted by DFT-based quasiharmonic approach, i.e., Helmholtz energy F for a given phase as a function of volume V and temperature T is determined by ^{71,72},

$$F(V, T) = E(V) + E_{vib}(V, T) + E_{el}(V, T) - T[S_{vib}(V, T) + S_{el}(V, T) + S_{conf}] \quad \text{Eq. 3}$$

Correspondingly, the Gibbs energy can be evaluated by $G(P, T) = F(V, T)|_{P=fix} + PV$ at the given pressure of interest. Here, $E_{vib}(V, T)$ and $S_{vib}(V, T)$ are vibrational contributions (internal energy and entropy, respectively) determined by phonon densities of states (DOS's, about 6 volumes were calculated for each phase)^{71,73}. $E_{el}(V, T)$ and $S_{el}(V, T)$ are thermal electronic contributions (internal energy and entropy, respectively) determined by electronic DOS's^{71,73}. S_{conf} is ideal configurational entropy for the IMCs with partially occupied Wyckoff sites, i.e., Al_5Fe_2 (described by Eq. 1) and Al_2Fe (Eq. 2),

$$S_{conf}^{Al_5Fe_2} = -\frac{4R(y_{Al}^b \log(y_{Al}^b) + y_{Va}^b \log(y_{Va}^b))}{24} - \frac{8R(y_{Al}^f \log(y_{Al}^f) + y_{Va}^f \log(y_{Va}^f))}{24} \quad \text{Eq. 4}$$

$$S_{conf}^{Al_2Fe} = -\frac{4R(y_{Al}^i \log(y_{Al}^i) + y_{Fe}^i \log(y_{Fe}^i))}{38} \quad \text{Eq. 5}$$

where R is gas constant and y the site fraction with the superscript being Wyckoff site (sublattice). Based on experimental measurements for Al_5Fe_2 ⁵⁸, $y_{Al}^b = 0.32$ ($y_{Al}^f = 0.24$) and $y_{Va}^b = 0.68$ ($y_{Va}^f = 0.76$) for Al and Va, respectively. Correspondingly, $y_{Al}^i = 0.295$ and $y_{Fe}^i = 0.705$ based on experiments for Al_2Fe ⁵⁹.

$E(V)$ in Eq. 3 is the static energy at 0 K without the zero-point vibrational energy, which was determined by fitting the DFT calculated energy-volume (E - V) data points using a four-parameter Birch-Murnaghan equation of state (EOS)⁷¹,

$$E(V) = k_1 + k_2V^{-2/3} + k_3V^{-4/3} + k_4V^{-2} \quad \text{Eq. 6}$$

where k_1 , k_2 , k_3 , and k_4 are fitting parameters. Equilibrium properties for each phase from this EOS include the equilibrium energy E_0 , volume V_0 , bulk modulus B_0 , and the pressure derivative of

bulk modulus B' . Usually, eight reliable data points were used for each EOS fitting in the present work.

2.3 Details of first-principles calculations

All DFT-based first-principles calculations in the present work were performed by the Vienna *Ab initio* Simulation Package (VASP) ⁷⁴ with the ion-electron interaction described by the projector augmented wave method ⁷⁵ and the exchange-correlation functional described by the generalized gradient approximation (GGA) developed by Perdew, Burke, and Ernzerhof (PBE) ⁷⁶. The same as those in the Materials Project ⁶¹, three electrons ($3s^23p^1$) were treated as valence electrons for Al and fourteen ($3p^63d^74s^1$) for Fe. In the VASP calculations, a plane wave cutoff energy of 293.2 eV was employed for structural relaxations and phonon calculations in terms of the Methfessel-Paxton method ⁷⁷. Final calculations of total energies and electronic DOS's were performed by the tetrahedron method with a Blöchl correction ⁷⁸ using a wave cutoff energy of 520 eV. The employed k -points meshes for each structure are listed in the Supplementary Table S 1. The self-consistency of total energy was converged to at least 10^{-6} eV/atom. Due to the magnetic nature of Fe, all Fe-containing materials were performed by the spin polarization calculations.

Phonon calculations were performed for each structure using the supercell approach ⁷⁹ in terms of the YPHON code ⁸⁰. Here, the VASP code was again the computational engine in calculating force constants using the finite differences method. The employed supercell for each structure and the corresponding k -points meshes are given in the Supplementary Table S 1. In addition, the single crystal elastic constants C_{ij} 's in the Al-Fe system were determined by applying the stress-strain method with the non-zero strains being ± 0.01 ; see details in ^{81,82}. The aggregate properties for

polycrystal were determined by using the Hill (H) approach^{83,84} based on the C_{ij} values, including bulk modulus (B_H), shear modulus (G_H), B_H/G_H ratio, Poisson's ratio (ν_H), and the anisotropy index A^U ⁸⁵. Note that the suggested DFT settings by USPEX^{60,64} were used in the present work, aiming at searching for the low energy configurations of Al_5Fe_2 by USPEX.

2.4 Formation of non-equilibrium IMCs through thermodynamic analysis

The decrease in Gibbs energy, $-\Delta G_m^\alpha$, for the precipitation of a new phase α (e.g., IMC) from a supersaturated solution (e.g., the supercooled liquid), is the thermodynamic driving force of formation, D , of the new α phase, i.e., $D = -\Delta G_m^\alpha$ ⁸⁶. The IMC with the highest thermodynamic driving force of formation can be selected as the IMC that would form first, making the driving force D a reasonable criterion to predict the first-forming IMC⁵². Similarly to the analysis of interface phases formed at the Cu/solder joints by Lee et al.⁵², for example, **Figure 1** shows that at 1000 K of the Al-Fe system, the supercooled liquid has a composition $x_{Fe} = 0.163$ (mole fraction of Fe in the metastable liquidus), which is in equilibrium with the supersaturated BCC phase (i.e., the metastable solidus) with $x_{Fe} = 0.281$. At this composition ($x_{Fe} = 0.281$), we can calculate thermodynamic driving forces of the IMCs (such as $Al_{13}Fe_4$, Al_5Fe_2 , Al_2Fe , and Al_8Fe_5) formed from the supersaturated BCC phase — the higher the driving force, the larger the possibility to form this IMC. In the present work, thermodynamic driving forces of the formation of IMCs from the supersaturated BCC phase were calculated as a function of temperature using the modeled Al-Fe system by Sundman et al.⁹ and the Thermo-Calc software⁵⁵.

In addition to thermodynamic driving force, we can also use the non-equilibrium phase diagram,

predicted by the Scheil-Gulliver simulations^{47,48} (see its definition in the Introduction section), to predict the formation of IMCs in fast cooling processes, such as the AM process^{49,50}. Here, we used the PyCalphad software^{50,87} to calculate this non-equilibrium phase diagram with the thermodynamic description modelled by Sundman et al.⁹.

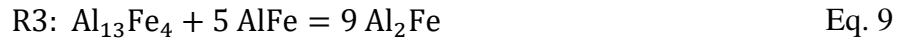
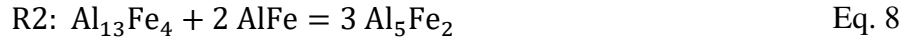
3 Results and Discussion

3.1 DFT-based phase stability of IMCs with respect to temperature and pressure

Figure 3 shows the predicted values of enthalpy of formation (ΔH_0) for the Al-Fe IMCs based on the present DFT calculations at $T = 0$ K and $P = 0$ GPa. Detailed atomic configuration and ΔH_0 value of each IMC are given in the Supplementary Table S 1; especially the predicted 14-atom configuration of Al_5Fe_2 by USPEX^{60,64} is listed in the Supplementary Table S 2. In addition, **Figure 3** shows also the convex hull by DFT calculations to display the stable IMCs, the experimental ΔH_0 values collected by Sundman et al.⁹ to measure the quality of the present DFT calculations, and the unstable configurations judged by imaginary phonon modes (not shown). It is seen (in **Figure 3**) that (i) the DFT-predicted ΔH_0 values agree well with the experimental data which are scattered; (ii) Al_6Fe is close to but above the convex hull, indicating that it is metastable at $T = 0$ K and $P = 0$ GPa, and more attentions need to be paid for its phase stability at high temperatures and high pressures; (iii) Al_9Fe_2 is an unstable structure and hence ignored in the present work; (iv) Al_5Fe_2 is a metastable phase at $T = 0$ K and $P = 0$ GPa, albeit various configurations have been examined in the present work (see the green open squares as well as the details in Table S 1); (v) the MoSi_2 -type Al_2Fe possesses the lowest energy and on the convex hull at $T = 0$ K and $P = 0$ GPa; and (vi) the IMCs of $\text{Al}_{13}\text{Fe}_4$, AlFe , and AlFe_3 are stable phases based on the convex hull. **Figure 3** implies that, at the conditions of $T = 0$ K and $P = 0$ GPa, the presently

predicted ΔH_0 values for Al_5Fe_2 and non- MoSi_2 -type Al_2Fe (i.e., the triclinic Al_2Fe ⁵⁹) are close to but above the convex hull, indicating that (a) the supercells used herein may be too small to search for the stable atomic configurations, and (b) more effects on phase stability such as temperature and pressure need to be considered. To this end as well as the suggestions by **Figure 3**, phase stabilities of Al_6Fe , Al_5Fe_2 , and Al_2Fe are further examined at finite temperatures and finite pressures (see **Figure 4**).

Figure 4 shows the changes of Gibbs energy, ΔG_{reac} , as a function of temperature and pressure ($P = 0$ and 6 GPa as two examples) for the following three reactions,



Here we choose the stable phases of Al, $\text{Al}_{13}\text{Fe}_4$, and AlFe (the B2 structure) as the reference states to examine phase stability of Al_6Fe , Al_5Fe_2 (using the configuration predicted by USPEX), and Al_2Fe (using the MoSi_2 -type configuration predicted by SIFPENN). It shows that Al_6Fe is a T -unfavored (see R1 in **Figure 4a**), but it is a P -favored phase (see R1 in **Figure 4b**). Phase stability of Al_6Fe (as well as other IMCs) at finite temperatures and under a given pressure can be understood by vibrational entropy, S_{vib} , in terms of the phonon density of states (DOS), $g(\omega)$ ⁸⁸,

$$S_{\text{vib}} \propto \int g(\omega) \ln(\omega) d\omega \quad \text{Eq. 10}$$

where ω is phonon frequency. Eq. 10 indicates that the higher the phonon DOS in the low ω region, the higher the S_{vib} contribution to Gibbs energy will be (see Eq. 3)^{54,88,89}. **Figure 5** shows the phonon DOS's of FCC Al and the selected Al-Fe IMCs at $P = 0$ GPa. In general, it shows that

the $g(\omega)$ of Al has the highest density than Al-Fe IMCs at the low frequency region (e.g., $\omega < 6$ THz), since FCC Al is the softest material with the largest equilibrium volume V_0 and the smallest bulk modulus B_0 in the Al-Fe system; see the Supplementary Table S 1. Relevant to the reaction R1 (Eq. 7) and at the low frequency region ($\omega < 6$ THz), **Figure 5** shows that the $g(\omega)$ of Al is much higher than that of Al₆Fe with $3.5 < \omega < 6$ THz, but the $g(\omega)$ of Al₆Fe has higher values in a small region with $\omega < 2$ THz. In addition, the phonon DOS's of Al and Al₁₃Fe₄ do not have significant differences at the low frequency region. These features imply that the S_{vib} contributions to both Al and Al₁₃Fe₄ should be slightly higher than that of Al₆Fe, resulting a slight increase of ΔG_{reac} for reaction R1 with increasing temperature (at $P = 0$ GPa). At higher pressures such as $P = 6$ GPa, ΔG_{reac} for reaction R1 keeps roughly constant since the S_{vib} contributions to both Al and Al₁₃Fe₄ are nearly identical to that of Al₆Fe. **Figure 4b** shows that with increasing pressure (even less than 1 GPa) instead of increasing temperature, Al₆Fe becomes stable with respect to Al and Al₁₃Fe₄ (*cf.*, the reaction R1). Based on experimental observations such as the examples #1 to #5 in **Table 1**, Al₆Fe was formed in the processes associated with pressures (such as die casting and equal channel angular extrusion) and in high Al-containing samples (e.g., $x_{\text{Al}} > 0.9$).

The reaction R2 (see Eq. 8) in **Figure 4a** and b shows that Al₅Fe₂ is a T -unfavored but P -favored phase by ignoring the contribution of configurational entropy S_{conf} ; see Eq. 3 and Eq. 4. The T -unfavored Al₅Fe₂ is due mainly to the lower phonon DOS of Al₅Fe₂ compared to that of AlFe with frequency ω around 4 THz (**Figure 5**). With S_{conf} contribution to ΔG_{reac} for reaction R2, Al₅Fe₂ becomes both the T - and P -favored phase (see the blue dash lines of R2). These results indicate that the factors, including atomic configuration, temperature, pressure, and S_{conf} , make Al₅Fe₂ more stable.

Figure 4 shows that the MoSi₂-type Al₂Fe is *T*-unfavored, but it is a strong *P*-favored phase. In addition, the S_{conf} has less contribution to ΔG_{reac} in comparison with that for Al₅Fe₂, due to the less partially occupied Wyckoff site of Al₂Fe; see Eq. 4 and Eq. 5. The *T*-unfavored behavior is caused by the lower phonon DOS of Al₂Fe than those of AlFe and Al₁₃Fe₄; see the ω range from 2 to 7 THz (**Figure 5**). With increasing pressure, **Figure 4** shows that the ΔG_{reac} value of reaction R3 decreases greatly; for example, dropping more than 2 kJ/mol-atom at $T = 0$ K as well as at other temperatures. Experimentally, the MoSi₂-type Al₂Fe was synthesized through the laser-heated diamond-anvil cell at 10 GPa and 1873 K⁹⁰, and it was suggested that it is a high pressure phase existed with $P > 5$ GPa⁶⁶; agreeing with the present conclusion that Al₂Fe is a *T*-unfavored but a strong *P*-favored phase, albeit it is stable at $T = 0$ K and $P = 0$ GPa (**Figure 3**).

Figure 6 shows a schematic *P-T* phase diagram (demonstrated with $P = 0$ and 6 GPa) for the Al-Fe system based on the present DFT calculations using Eq. 3. It shows that Al₁₃Fe₄, AlFe, and AlFe₃ are already the stable IMCs marked by the shaded regions. However, at low pressures and low temperatures (e.g., $P = 0$ GPa and $T < 165$ K), the L1₂-type AlFe₃ is more stable than the D0₃-type AlFe₃. In all temperature range in **Figure 6**, Al₆Fe is not stable when $P = 0$ GPa but stable at higher pressures. Al₅Fe₂ (configuration predicted by USPEX) is stable at high temperatures (e.g., $T > 345$ K with $P = 0$ GPa), while the pressure decreases its stability slightly. The MoSi₂-type Al₂Fe is a *T*-unfavored but a strong *P*-favored phase.

Table 2 summarizes phase stability of Al-Fe IMCs as a function of pressure and temperature as shown in **Figure 1**, **Figure 3**, and **Figure 6**; together with their ductility/brittleness judged by

Pugh's criterion ^{11,12} as shown in **Figure 2**, which were determined by the presently predicted elastic constants in Table S 3.

3.2 Phase stability of Al-Fe IMCs by thermodynamic and kinetic analyses

Figure 7 shows the predicted thermodynamic driving forces of the Al-Fe IMCs in the temperature range, $920 \text{ K} < T < 1320 \text{ K}$, together with the associated mole fraction of Fe (x_{Fe}) along the metastable solidus line in **Figure 1**. Note that the eutectic reaction temperature is 927 K and the used thermodynamic description was modelled by Sundman et al. ⁹. It is seen that both $\text{Al}_{13}\text{Fe}_4$ and Al_5Fe_2 have the higher thermodynamic driving forces of formation at lower temperatures ($< 1280 \text{ K}$) than those of Al_2Fe and Al_8Fe_5 . By examining atomic diffusivity in Al-Fe IMCs, the interdiffusion coefficients in Al_5Fe_2 are at least two orders of magnitude faster than those in the other IMCs (AlFe , Al_2Fe , and $\text{Al}_{13}\text{Fe}_4$) at $T = 823 - 913 \text{ K}$ ⁴⁰; and they are comparable with the diffusion coefficients of dilute Fe in FCC Al; see **Figure 8** based on diffusion coefficients reported in the literature ^{40,56,57}. In addition, Al atoms have higher diffusivity in Al_5Fe_2 than Fe atoms ³⁶. The fastest atomic diffusivity, especially Al atoms, in Al_5Fe_2 is due mainly to the rich Al vacancies in Al_5Fe_2 ⁵⁸; see Eq. 1. However, considerable vacancies have not been reported in the other Al-Fe IMCs. By considering both the high thermodynamic driving force of formation (**Figure 7**) and the fastest interdiffusion coefficients (**Figure 8**), the brittle Al_5Fe_2 is the IMC with the largest possibility to be formed; see the Al-rich examples in Table 1, except for the samples with extremely high Al contents, or formed below the eutectic reaction temperature of 927 K, or processed by AM (examples #1 to #5, and #7 to #11).

As two examples, **Figure 9** shows the calculated mole fractions of solid phases by Scheil

simulations using the thermodynamic description modelled by Sundman et al. ⁹. With decreasing temperature at the fixed composition of $x_{\text{Fe}} = 0.3$, the solid phase of Al_5Fe_2 forms first and reaches a maximum mole fraction about 0.5 at $T = 1427.5$ K, and then the second solid phase of Al_8Fe_5 forms at almost the fixed temperature of 1427.5 K. Due to the extremely small temperature range ($\ll 1$ K) for phase transition, Al_8Fe_5 was not observed in all the processes in Table 1. For the case of $x_{\text{Fe}} = 0.6$, the first formed solid phase is BCC (or B2 phase) with decreasing temperature and reaches a maximum mole fraction of 0.95, and then Al_8Fe_5 forms in a small temperature range of 1505 ~ 1493 K. Similar to the case of $x_{\text{Fe}} = 0.3$, the predicted Al_8Fe_5 was also not observed in the processes in Table 1 due probably to the small temperature range of phase formation. **Figure 10** shows the complete non-equilibrium phase diagram by Scheil simulations using the modelled Al-Fe system by Sundman et al. ⁹. This non-equilibrium phase diagram shows the temperatures of the forming phases, while the lever rule cannot be used to determine phase fractions. Both the equilibrium phase diagram (**Figure 1**) and the Schiel non-equilibrium phase diagram (**Figure 10**) can be used to determine the forming phases in the slow/equilibrium and the fast cooling processes, respectively.

As an example, **Figure 11** show the forming phases as a function of temperature with $x_{\text{Fe}} = 0.4$. The forming phases are BCC (minor) and Al_8Fe_5 (major) based on Schiel simulations (see also **Figure 10**), while the forming phases are Al_8Fe_5 (when $T > 1360$ K), BCC, and Al_2Fe based on equilibrium calculations (see also **Figure 1**). Therefore, the forming phases could be BCC, Al_2Fe , and/or Al_8Fe_5 depended on the processes. For instance, Stein et al. ⁹¹ observed the eutectoid reaction of $\text{Al}_8\text{Fe}_5 \leftrightarrow \text{Al}_2\text{Fe} + \text{BCC (B2)}$ at 1368 K according to the differential thermal analyses for the Al-40 at.% Fe alloy ($x_{\text{Fe}} = 0.4$) at the heating rates of 5 and 10 K/min.

It should be mentioned that the forming phases depend mainly on compositions (especially the local compositions) in addition to temperature, pressure, and atomic diffusivity for the system of interest. Table 1 shows that AM is a superior process than the other processes to achieve desired phases such as AlFe and AlFe₃ through varying the compositions. Aiming to predict the forming IMCs under a given composition and a given processing history, the combined thermodynamic and kinetic simulations are needed. For example, Lindwall et al.⁹² simulated the time-temperature-transformation (TTT) diagram and the forming IMCs in the additively manufactured Ni-based Inconel 625. However, these simulations are beyond the scope of the present work.

4 Summary

The present work investigated the forming mechanism of equilibrium and non-equilibrium intermetallic compounds (IMCs) in aluminum/steel (Al-Fe) joints by means of Gibbs energy as a function of temperature (T) and pressure (P) from (i) the first-principles phonon calculations, (ii) the equilibrium Al-Fe phase diagram in the literature and the presently predicted non-equilibrium phase diagram by Scheil simulations, (iii) atomic diffusivity in Al-Fe, and (iv) experimentally observed IMCs in various processes. Specially, the unknown atomic configurations of Al₂Fe and Al₅Fe₂ were examined in the present work by machine learning based datamining together with first-principles verifications and structure predictor (using USPEX).

We conclude that the formation of IMCs can be explained well by using phase diagrams, thermodynamic driving forces, P - and T -included Gibbs energy, and atomic diffusion coefficients.

Specifically, the metastable while ductile Al_6Fe is a P -favored IMC, which was observed in Al-dominant samples and the processes involving pressures such as direct-chill casting, die casting, equal channel angular extrusion. Here the ductility and brittleness of IMCs were judged by Pugh's criterion^{11,12} using the presently predicted elastic constants. The MoSi_2 -type Al_2Fe is a brittle and a strong P -favored IMC observed at high pressures. The stable but brittle $\eta\text{-Al}_5\text{Fe}_2$ is the most observed IMC usually adjacent to steel (Fe) in almost all the processes (see Table 1), such as the fusion or solid-state welding, immersion test, diffusion couple, and additive manufacturing (AM), since Al_5Fe_2 is a T -favored phase with a high thermodynamic driving force of formation and the fastest atomic diffusivity among all Al-Fe IMCs. The slightly brittle $\theta\text{-Al}_{13}\text{Fe}_4$ is the second most observed IMC usually adjacent to Al shown in most of the processes, which possesses the highest thermodynamic driving force of formation in Al-rich side. Notably the ductile AlFe_3 , the less ductile AlFe , and almost all the other IMCs were observed in the AM processes, making AM an exceptional way to tailor composition and in turn achieve the desired IMCs in dissimilar materials. All the IMCs (without the P -favored phases) formed in the Al-Fe joints can be identified using the equilibrium and the Scheil non-equilibrium phase diagrams, together with kinetic considerations.

Declaration of Competing Interest

The authors declare that they have no known competing financial interests or personal relationships that could have appeared to influence the work reported in this paper.

Acknowledgments

The authors acknowledge the financial support partially by the U.S. Department of Energy (DOE) via Award No. DE-EE0008456; and partially by the National Science Foundation (NSF) with Grant No. CMMI-1825538. First-principles calculations were performed partially on the Roar supercomputer at the Pennsylvania State University's Institute for Computational and Data Sciences (ICDS), partially on the resources of the National Energy Research Scientific Computing Center (NERSC) supported by the U.S. DOE Office of Science User Facility operated under Contract No. DE-AC02-05CH11231, and partially on the resources of the Extreme Science and Engineering Discovery Environment (XSEDE) supported by NSF with Grant No. ACI-1548562.

References:

1. Wang, P., Chen, X., Pan, Q., Madigan, B. & Long, J. Laser welding dissimilar materials of aluminum to steel: an overview. *Int. J. Adv. Manuf. Technol.* **87**, 3081–3090 (2016).
2. Sakundarini, N., Taha, Z., Abdul-Rashid, S. H. & Ghazila, R. A. R. Optimal multi-material selection for lightweight design of automotive body assembly incorporating recyclability. *Mater. Des.* **50**, 846–857 (2013).
3. Wargnier, H., Kromm, F. X., Danis, M. & Brechet, Y. Proposal for a multi-material design procedure. *Mater. Des.* **56**, 44–49 (2014).
4. Bahraminasab, M. *et al.* Multi-objective design optimization of functionally graded material for the femoral component of a total knee replacement. *Mater. Des.* **53**, 159–173 (2014).
5. Aizawa, T., Okagawa, K. & Kashani, M. Application of magnetic pulse welding technique for flexible printed circuit boards (FPCB) lap joints. *J. Mater. Process. Technol.* **213**, 1095–1102 (2013).
6. Springer, H., Kostka, A., dos Santos, J. F. & Raabe, D. Influence of intermetallic phases and Kirkendall-porosity on the mechanical properties of joints between steel and aluminium alloys. *Mater. Sci. Eng. A* **528**, 4630–4642 (2011).
7. Safeen, M. W. & Russo Spena, P. Main Issues in Quality of Friction Stir Welding Joints of Aluminum Alloy and Steel Sheets. *Metals (Basel)*. **9**, 610 (2019).
8. Hussein, S. A., Tahir, A. S. M. & Hadzley, A. B. Characteristics of aluminum-to-steel joint made by friction stir welding: A review. *Mater. Today Commun.* **5**, 32–49 (2015).
9. Sundman, B., Ohnuma, I., Dupin, N., Kattner, U. R. & Fries, S. G. An assessment of the entire Al–Fe system including D03 ordering. *Acta Mater.* **57**, 2896–2908 (2009).

10. Aliravci, C. A. & Pekgülyüz, M. Ö. Calculation of phase diagrams for the metastable Al-Fe phases forming in direct-chill (DC)-cast aluminum alloy ingots. *Calphad* **22**, 147–155 (1998).
11. Pugh, S. F. XCII. Relations between the elastic moduli and the plastic properties of polycrystalline pure metals. *Philos. Mag.* **45**, 823–843 (1954).
12. Liu, Z. Q. *et al.* Electrically reversible cracks in an intermetallic film controlled by an electric field. *Nat. Commun.* **9**, 41 (2018).
13. Zhu, X., Blake, P. & Ji, S. The formation mechanism of Al₆(Fe, Mn) in die-cast Al-Mg alloys. *CrystEngComm* **20**, 3839–3848 (2018).
14. Yu, F., Liu, F., Zhao, D. & Toth, L. S. Microstructure and mechanical properties of Al-3Fe alloy processed by equal channel angular extrusion. in *IOP Conference Series: Materials Science and Engineering* vol. 63 012079 (Institute of Physics Publishing, 2014).
15. He, H., Lin, S., Yang, C., Fan, C. & Chen, Z. Combination Effects of Nocolok Flux with Ni Powder on Properties and Microstructures of Aluminum-Stainless Steel TIG Welding-Brazing Joint. *J. Mater. Eng. Perform.* **22**, 3315–3323 (2013).
16. Qi, X., Takata, N., Suzuki, A., Kobashi, M. & Kato, M. Laser powder bed fusion of a near-eutectic Al-Fe binary alloy: Processing and microstructure. *Addit. Manuf.* **35**, 101308 (2020).
17. Shishkovsky, I., Missemer, F., Kakovkina, N. & Smurov, I. Intermetallics Synthesis in the Fe-Al System via Layer by Layer 3D Laser Cladding. *Crystals* **3**, 517–529 (2013).
18. Pęska, M., Karczewski, K., Rzeszotarska, M. & Polański, M. Direct Synthesis of Fe-Al Alloys from Elemental Powders Using Laser Engineered Net Shaping. *Materials (Basel)*. **13**, 531 (2020).

19. Lotfian, S., Rolink, G., Weisheit, A. & Palm, M. Chemically graded Fe-Al/steel samples fabricated by laser metal deposition. in *MRS Advances* vol. 2 1393–1398 (Materials Research Society, 2017).
20. Shen, C., Pan, Z., Cuiuri, D., Roberts, J. & Li, H. Fabrication of Fe-FeAl Functionally Graded Material Using the Wire-Arc Additive Manufacturing Process. *Metall. Mater. Trans. B Process Metall. Mater. Process. Sci.* **47**, 763–772 (2016).
21. Shen, C., Pan, Z., Ma, Y., Cuiuri, D. & Li, H. Fabrication of iron-rich Fe-Al intermetallics using the wire-arc additive manufacturing process. *Addit. Manuf.* **7**, 20–26 (2015).
22. Yamagiwa, K., Watanabe, Y., Fukui, Y. & Kapranos, P. Novel recycling system of aluminum and iron wastes-in-situ Al-Al₃Fe functionally graded material manufactured by a centrifugal method. *Mater. Trans.* **44**, 2461–2467 (2003).
23. Fan, J., Thomy, C. & Vollertsen, F. Effect of thermal cycle on the formation of intermetallic compounds in laser welding of aluminum-steel overlap joints. in *Physics Procedia* vol. 12 134–141 (Elsevier B.V., 2011).
24. Wang, C. *et al.* The influence of heat input on microstructure and mechanical properties for dissimilar welding of galvanized steel to 6061 aluminum alloy in a zero-gap lap joint configuration. *J. Alloys Compd.* **726**, 556–566 (2017).
25. Meco, S., Ganguly, S., Williams, S. & McPherson, N. Effect of laser processing parameters on the formation of intermetallic compounds in Fe-Al dissimilar welding. *J. Mater. Eng. Perform.* **23**, 3361–3370 (2014).
26. Elrefaey, A., Gouda, M., Takahashi, M. & Ikeuchi, K. Characterization of aluminum/steel lap joint by friction stir welding. *J. Mater. Eng. Perform.* **14**, 10–17 (2005).
27. Abbasi, M., Dehghani, M., Guim, H. U. & Kim, D. I. Investigation of Fe-rich fragments in

- aluminum-steel friction stir welds via simultaneous Transmission Kikuchi Diffraction and EDS. *Acta Mater.* **117**, 262–269 (2016).
28. Das, H., Ghosh, R. N. & Pal, T. K. Study on the formation and characterization of the intermetallics in friction stir welding of aluminum alloy to coated steel sheet lap joint. in *Metallurgical and Materials Transactions A: Physical Metallurgy and Materials Science* vol. 45 5098–5106 (Springer Boston, 2014).
 29. Haghshenas, M. *et al.* Friction stir weld assisted diffusion bonding of 5754 aluminum alloy to coated high strength steels. *Mater. Des.* **55**, 442–449 (2014).
 30. Movahedi, M. *et al.* Growth kinetics of Al-Fe intermetallic compounds during annealing treatment of friction stir lap welds. *Mater. Charact.* **90**, 121–126 (2014).
 31. Taban, E., Gould, J. E. & Lippold, J. C. Dissimilar friction welding of 6061-T6 aluminum and AISI 1018 steel: Properties and microstructural characterization. *Mater. Des.* **31**, 2305–2311 (2010).
 32. Bozzi, S., Helbert-Etter, A. L., Baudin, T., Criqui, B. & Kerbiguet, J. G. Intermetallic compounds in Al 6016/IF-steel friction stir spot welds. *Mater. Sci. Eng. A* **527**, 4505–4509 (2010).
 33. Wang, K. *et al.* Investigation of Interfacial Layer for Friction Stir Scribe Welded Aluminum to Steel Joints. *J. Manuf. Sci. Eng.* **140**, (2018).
 34. Najafi, A., Movahedi, M. & Yarandi, A. S. Properties–microstructure relationship in Al–Fe in situ composite produced by friction stir processing. *Proc. Inst. Mech. Eng. Part L J. Mater. Des. Appl.* **233**, 1955–1965 (2019).
 35. Agudo, L. *et al.* Intermetallic Fe x Al y -phases in a steel/Al-alloy fusion weld. *J. Mater. Sci.* **42**, 4205–4214 (2007).

36. Zhang, G., Chen, M., Shi, Y., Huang, J. & Yang, F. Analysis and modeling of the growth of intermetallic compounds in aluminum-steel joints. *RSC Adv.* **7**, 37797–37805 (2017).
37. Ding, Z. *et al.* Microstructural evolution and growth behavior of intermetallic compounds at the liquid Al/solid Fe interface by synchrotron X-ray radiography. *Mater. Charact.* **136**, 157–164 (2018).
38. Bouché, K., Barbier, F. & Coulet, A. Intermetallic compound layer growth between solid iron and molten aluminium. *Mater. Sci. Eng. A* **249**, 167–175 (1998).
39. Bouayad, A., Gerometta, C., Belkebir, A. & Ambari, A. Kinetic interactions between solid iron and molten aluminium. *Mater. Sci. Eng. A* **363**, 53–61 (2003).
40. Naoi, D. & Kajihara, M. Growth behavior of Fe₂Al₅ during reactive diffusion between Fe and Al at solid-state temperatures. *Mater. Sci. Eng. A* **459**, 375–382 (2007).
41. Tanaka, Y. & Kajihara, M. Kinetics of isothermal reactive diffusion between solid Fe and liquid Al. *J. Mater. Sci.* **45**, 5676–5684 (2010).
42. Wang, X., Wood, J. V., Sui, Y. & Lu, H. Formation of intermetallic compound in iron-aluminum alloys. *J. Shanghai Univ. (English Ed.)* **2**, 305–310 (1998).
43. Novák, P. *et al.* On the formation of intermetallics in Fe-Al system - An in situ XRD study. *Intermetallics* **32**, 127–136 (2013).
44. Van Alboom, A. *et al.* Multi-method identification and characterization of the intermetallic surface layers of hot-dip Al-coated steel: FeAl₃ or Fe₄Al₁₃ and Fe₂Al₅ or Fe₂Al_{5+x}. *Surf. Coatings Technol.* **324**, 419–428 (2017).
45. Liu, Z.-K. Computational thermodynamics and its applications. *Acta Mater.* **200**, 745–792 (2020).
46. Schmid-Fetzer, R. Phase Diagrams: The Beginning of Wisdom. *J. Phase Equilibria*

- Diffus.* **35**, 735–760 (2014).
47. Scheil, E. Bemerkungen zur schichtkristallbildung. *Zeitschrift für Met.* **34**, 70–72 (1942).
 48. Gulliver, G. H. The quantitative effect of rapid cooling upon the constitution of binary alloys. *J. Inst. Met* **9**, 120–157 (1913).
 49. Moustafa, A. R., Durga, A., Lindwall, G. & Cordero, Z. C. Scheil ternary projection (STeP) diagrams for designing additively manufactured functionally graded metals. *Addit. Manuf.* **32**, 101008 (2020).
 50. Bocklund, B., Bobbio, L. D., Otis, R. A., Beese, A. M. & Liu, Z.-K. Experimental validation of Scheil–Gulliver simulations for gradient path planning in additively manufactured functionally graded materials. *Materialia* **11**, 100689 (2020).
 51. Schaffnit, P., Stallybrass, C., Konrad, J., Stein, F. & Weinberg, M. A Scheil-Gulliver model dedicated to the solidification of steel. *Calphad Comput. Coupling Phase Diagrams Thermochem.* **48**, 184–188 (2015).
 52. Lee, H. M., Yoon, S. W. & Lee, B.-J. Thermodynamic prediction of interface phases at Cu/solder joints. *J. Electron. Mater.* **27**, 1161–1166 (1998).
 53. Zhou, S. H. & Napolitano, R. E. Energetics of nonequilibrium solidification in Al-Sm. *Phys. Rev. B* **78**, 184111 (2008).
 54. Wang, K. *et al.* Unveiling non-equilibrium metallurgical phases in dissimilar Al-Cu joints processed by vaporizing foil actuator welding. *Mater. Des.* **186**, 108306 (2020).
 55. Andersson, J.-O., Helander, T., Höglund, L., Shi, P. & Sundman, B. Thermo-Calc & DICTRA, computational tools for materials science. *Calphad* **26**, 273–312 (2002).
 56. Du, Y. *et al.* Diffusion coefficients of some solutes in fcc and liquid Al: Critical evaluation and correlation. *Mater. Sci. Eng. A* **363**, 140–151 (2003).

57. Helander, T. & Ågren, J. A phenomenological treatment of diffusion in Al–Fe and Al–Ni alloys having B2-b.c.c. ordered structure. *Acta Mater.* **47**, 1141–1152 (1999).
58. Burkhardt, U., Grin, Y., Ellner, M., Peters, K. & IUCr. Structure refinement of the iron–aluminium phase with the approximate composition Fe₂Al₅. *Acta Crystallogr. Sect. B Struct. Sci.* **50**, 313–316 (1994).
59. Chumak, I., Richter, K. W. & Ehrenberg, H. Redetermination of iron dialuminide, FeAl₂. *Acta Crystallogr. Sect. C Cryst. Struct. Commun.* **66**, i87–i88 (2010).
60. Lyakhov, A. O., Oganov, A. R., Stokes, H. T. & Zhu, Q. New developments in evolutionary structure prediction algorithm USPEX. *Comput. Phys. Commun.* **184**, 1172–1182 (2013).
61. Jain, A. *et al.* Commentary: The Materials Project: A materials genome approach to accelerating materials innovation. *APL Mater.* **1**, 011002 (2013).
62. Kirklin, S. *et al.* The Open Quantum Materials Database (OQMD): assessing the accuracy of DFT formation energies. *npj Comput. Mater.* **1**, 15010 (2015).
63. van de Walle, A. *et al.* Efficient stochastic generation of special quasirandom structures. *Calphad* **42**, 13–18 (2013).
64. Glass, C. W., Oganov, A. R. & Hansen, N. USPEX - Evolutionary crystal structure prediction. *Comput. Phys. Commun.* **175**, 713–720 (2006).
65. Vinokur, A. I., Hilleke, K. P. & Fredrickson, D. C. Principles of weakly ordered domains in intermetallics: The cooperative effects of atomic packing and electronics in Fe₂Al₅. *Acta Crystallogr. Sect. A Found. Adv.* **75**, 297–306 (2019).
66. Tobita, K. *et al.* Phase stability and thermoelectric properties of semiconductor-like tetragonal FeAl₂. *Sci. Technol. Adv. Mater.* **20**, 937–948 (2019).

67. Gražulis, S. *et al.* Crystallography Open Database – an open-access collection of crystal structures. *J. Appl. Crystallogr.* **42**, 726–729 (2009).
68. Gražulis, S. *et al.* Crystallography Open Database (COD): an open-access collection of crystal structures and platform for world-wide collaboration. *Nucleic Acids Res.* **40**, D420–D427 (2012).
69. Choudhary, K. *et al.* The joint automated repository for various integrated simulations (JARVIS) for data-driven materials design. *npj Comput. Mater.* **6**, 173 (2020).
70. Krajewski, A. M., Siegel, J. W., Xu, J. & Liu, Z.-K. Extensible Structure-Informed Prediction of Formation Energy with Improved Accuracy and Usability employing Neural Networks. *arXiv* arXiv:2008.13654 (2020).
71. Shang, S.-L., Wang, Y., Kim, D. & Liu, Z.-K. First-principles thermodynamics from phonon and Debye model: Application to Ni and Ni₃Al. *Comput. Mater. Sci.* **47**, 1040–1048 (2010).
72. Wang, A. *et al.* Effects of pressure and vibration on the thermal decomposition of cubic Ti_{1-x}Al_xN, Ti_{1-x}Zr_xN, and Zr_{1-x}Al_xN coatings: A first-principles study. *J. Mater. Sci.* **47**, 7621–7627 (2012).
73. Wang, Y., Liu, Z. K. & Chen, L. Q. Thermodynamic properties of Al, Ni, NiAl, and Ni₃Al from first-principles calculations. *Acta Mater.* **52**, 2665–2671 (2004).
74. Kresse, G. *et al.* Efficient iterative schemes for ab initio total-energy calculations using a plane-wave basis set. *Phys. Rev. B* **54**, 11169–11186 (1996).
75. Kresse, G. & Joubert, D. From ultrasoft pseudopotentials to the projector augmented-wave method. *Phys. Rev. B* **59**, 1758–1775 (1999).
76. Perdew, J. P., Burke, K. & Ernzerhof, M. Generalized Gradient Approximation Made

- Simple. *Phys. Rev. Lett.* **77**, 3865–3868 (1996).
77. Methfessel, M. & Paxton, A. T. High-precision sampling for Brillouin-zone integration in metals. *Phys. Rev. B* **40**, 3616–3621 (1989).
 78. Blöchl, P. E., Jepsen, O. & Andersen, O. K. Improved tetrahedron method for Brillouin-zone integrations. *Phys. Rev. B* **49**, 16223–16233 (1994).
 79. Wang, Y. *et al.* A mixed-space approach to first-principles calculations of phonon frequencies for polar materials. *J. Phys. Condens. Matter* **22**, 202201 (2010).
 80. Wang, Y., Shang, S.-L., Fang, H., Liu, Z.-K. & Chen, L.-Q. First-principles calculations of lattice dynamics and thermal properties of polar solids. *npj Comput. Mater.* **2**, 16006 (2016).
 81. Shang, S., Wang, Y. & Liu, Z.-K. First-principles elastic constants of α - and θ -Al₂O₃. *Appl. Phys. Lett.* **90**, 101909 (2007).
 82. Shang, S. L. *et al.* First-principles calculations of pure elements: Equations of state and elastic stiffness constants. *Comput. Mater. Sci.* **48**, 813–826 (2010).
 83. Hill, R. The Elastic Behaviour of a Crystalline Aggregate. *Proc. Phys. Soc. Sect. A* **65**, 349–354 (1952).
 84. Simmons, G. & Wang, H. *Single crystal elastic constants and calculated aggregate properties: A handbook*. (M.I.T. Press, 1971).
 85. Ranganathan, S. I. & Ostoja-Starzewski, M. Universal elastic anisotropy index. *Phys. Rev. Lett.* **101**, 055504 (2008).
 86. Hillert, M. *Phase equilibria, phase diagrams and phase transformations: Their thermodynamic basis*. (Cambridge University Press, 2008).
 87. Otis, R. & Liu, Z.-K. pycalphad: CALPHAD-based Computational Thermodynamics in

- Python. *J. Open Res. Softw.* **5**, 1 (2017).
88. Wolverton, C. & Ozoliņš, V. Entropically Favored Ordering: The Metallurgy of Al₂Cu Revisited. *Phys. Rev. Lett.* **86**, 5518–5521 (2001).
 89. Shang, S.-L., Wang, Y., Du, Y. & Liu, Z.-K. Entropy favored ordering: Phase stability of Ni₃Pt revisited by first-principles. *Intermetallics* **18**, 961–964 (2010).
 90. Tobita, K. *et al.* High-pressure synthesis of tetragonal iron aluminide FeAl₂. *Scr. Mater.* **141**, 107–110 (2017).
 91. Stein, F., Vogel, S. C., Eumann, M. & Palm, M. Determination of the crystal structure of the ϵ phase in the Fe-Al system by high-temperature neutron diffraction. *Intermetallics* **18**, 150–156 (2010).
 92. Lindwall, G. *et al.* Simulation of TTT Curves for Additively Manufactured Inconel 625. *Metall. Mater. Trans. A* **50**, 457–467 (2019).
 93. Okamoto, N. L., Okumura, J., Higashi, M. & Inui, H. Crystal structure of η' -Fe₃Al₈; low-temperature phase of η -Fe₂Al₅ accompanied by an ordered arrangement of Al atoms of full occupancy in the c-axis chain sites. *Acta Mater.* **129**, 290–299 (2017).

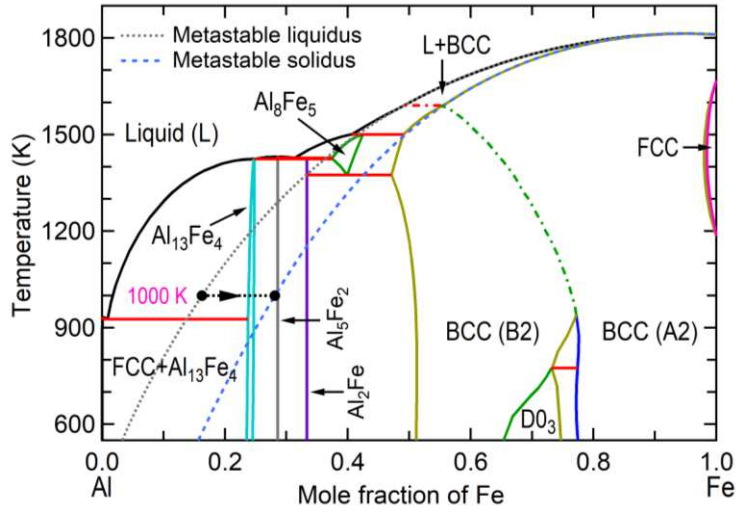


Figure 1. Calculated Al-Fe phase diagram based on CALPHAD modeling by Sundman et al. ⁹. The metastable liquidus and solidus lines are plotted to analyze the formation of non-equilibrium phases from the supersaturated solution phase; and one example at 1000 K is shown for phase equilibrium from the supercooled liquid with composition $x_{\text{Fe}} = 0.163$ to the supersaturated BCC phase with $x_{\text{Fe}} = 0.218$.

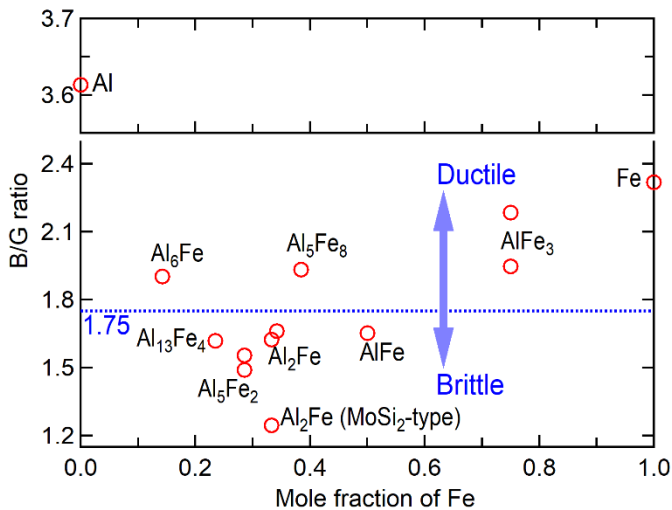


Figure 2. Calculated bulk modulus versus shear modulus (B/G) ratios of Al-Fe IMCs based on the present DFT calculations; see details in Table S 3. Note that the Pugh's criterion ¹¹ of 1.75 is a rough value to separate the ductile and brittle materials as discussed in the authors' responses to Reviewers in ¹².

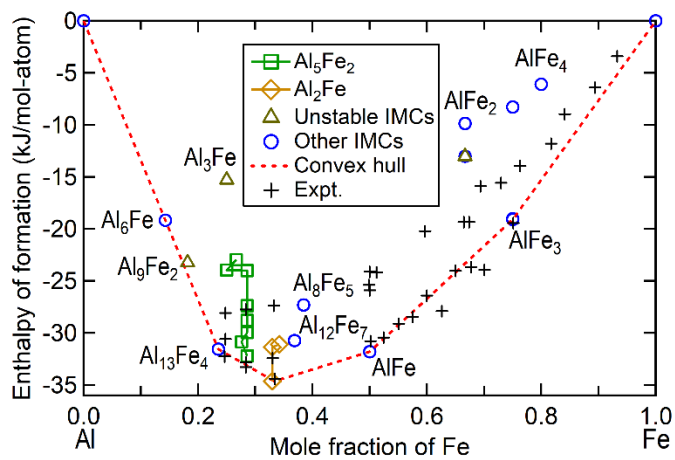


Figure 3. Predicted enthalpies of formation (ΔH_0) at $T = 0$ K and $P = 0$ GPa for Al-Fe IMCs by the present DFT calculations (see structural details and ΔH_0 values in Table S 1). Note that the convex hull was plotted using the DFT results, the unstable IMCs were judged by imaginary phonon modes, and the experimental data (Expt.) were collected by Sundman et al. ⁹.

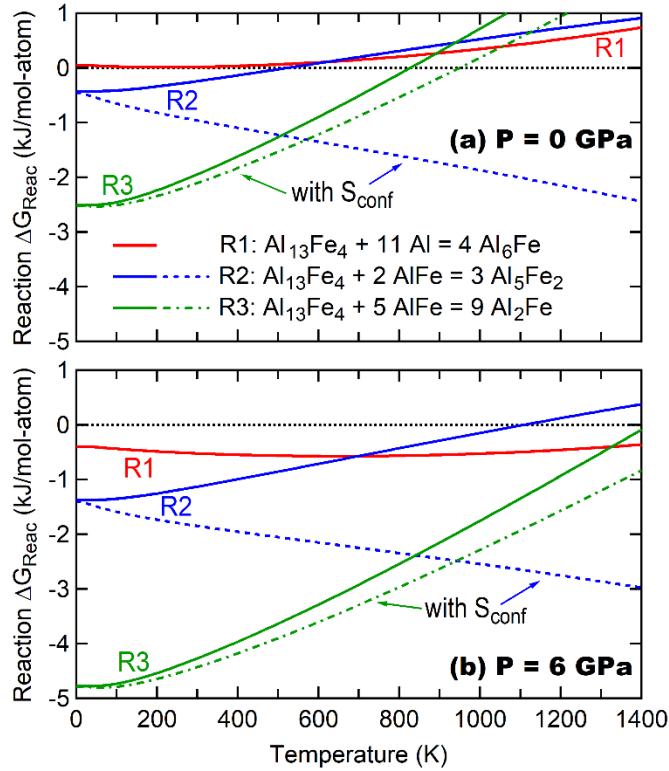


Figure 4. Reaction Gibbs energies (ΔG_{reac} 's) under external pressure $P = 0$ GPa (a) and 6 GPa (b) with and without considering the ideal configurational entropies (S_{conf} 's) of Al_5Fe_2 and Al_2Fe , respectively; see Eq. 4 and Eq. 5.

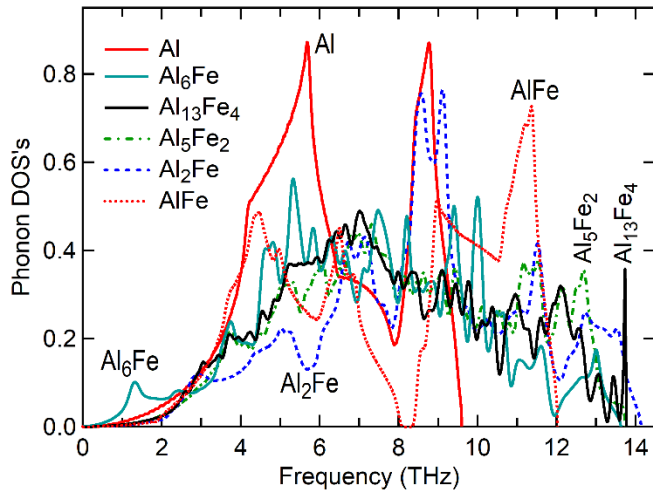


Figure 5. Calculated phonon densities of states (DOS's) of fcc Al and the selected IMCs of Al_6Fe , $\text{Al}_{13}\text{Fe}_4$, Al_5Fe_2 (predicted by USPEX), the MoSi_2 -type Al_2Fe , and AlFe (the B2 phase). Note that all phonon DOS's have the same integral value.

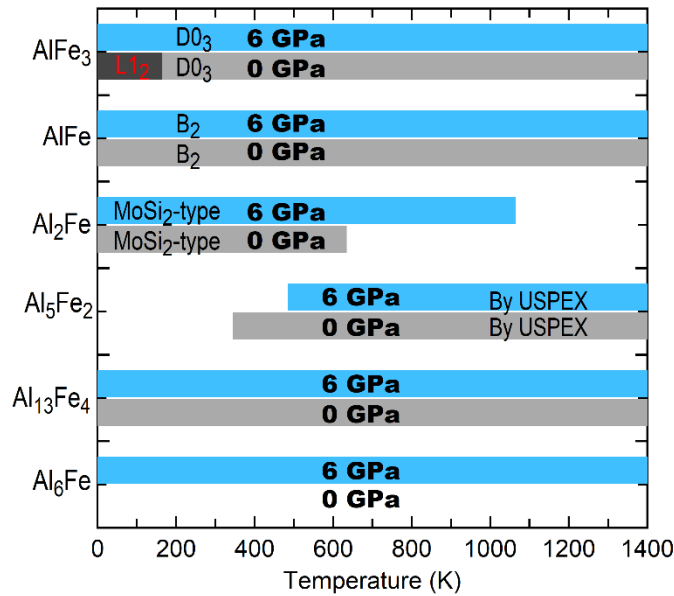


Figure 6. Phase stability (on the convex hull) of Al-Fe IMCs under external pressures of 0 and 6 GPa as a function of temperature (shown in the shaded regions) based on the present DFT calculations using Eq. 3.

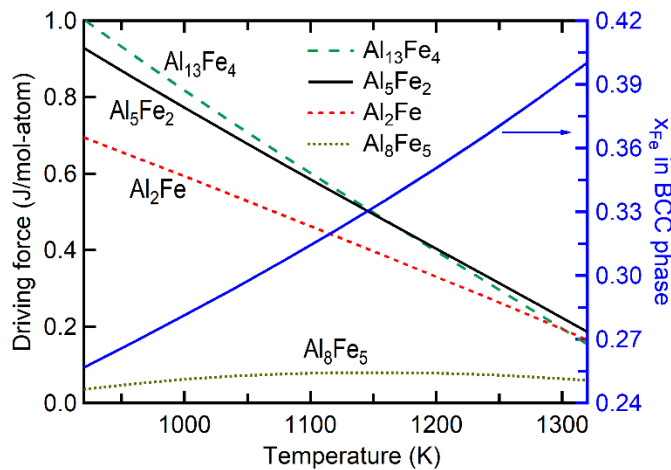


Figure 7. Thermodynamic driving forces the Al-Fe IMCs as a function of temperature together with the mole fraction of Fe (x_{Fe}) along the metastable BCC phase in **Figure 1**. Here, the used Al-Fe thermodynamic properties were modelled by Sundman et al. ⁹.

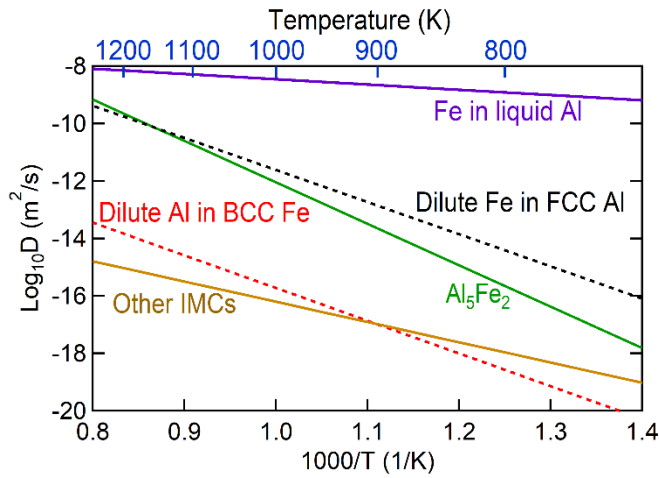


Figure 8. Diffusion coefficients of Fe in liquid Al ⁵⁶, dilute Fe in FCC Al ⁵⁶, dilute Al in BCC Fe ⁵⁷, and the elements in Al₅Fe₂ and other IMCs (AlFe, Al₂Fe, and Al₁₃Fe₄) ⁴⁰.

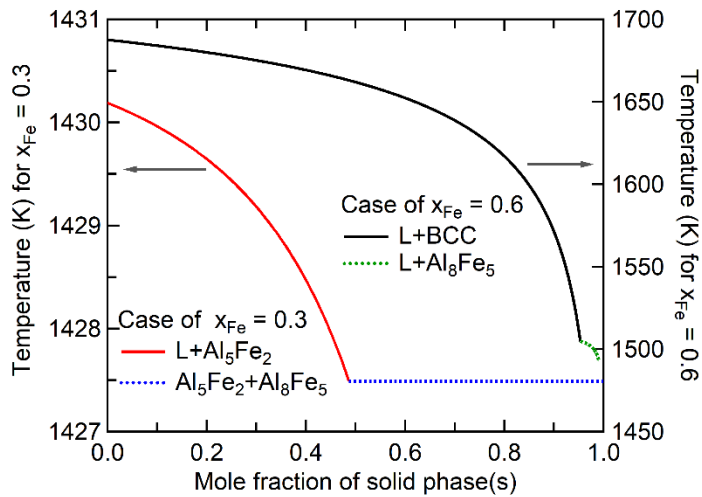


Figure 9. Calculated mole fractions of solid phases with $x_{Fe} = 0.3$ and 0.6 based on Scheil simulations using thermodynamic description modelled by Sundman et al. ⁹.

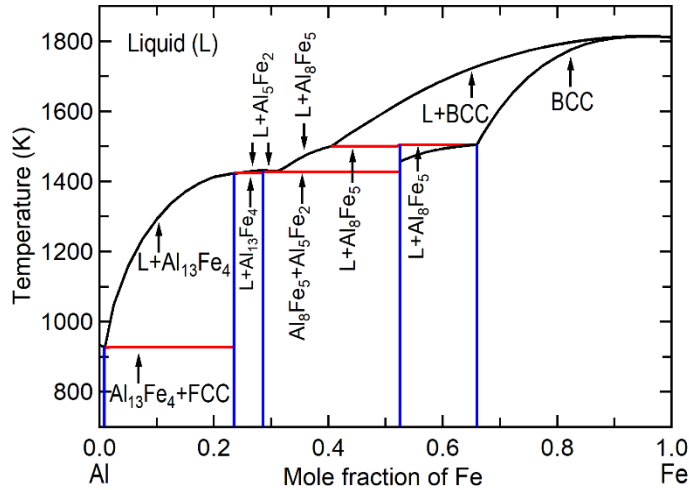


Figure 10. Predicted Al-Fe non-equilibrium phase diagram by Scheil simulations using the modelled data by Sundman et al.⁹, showing the forming temperatures for the phases indicated by the lines. Note that the lever rule cannot be used to determine phase fractions (see Figure 9 for two examples).

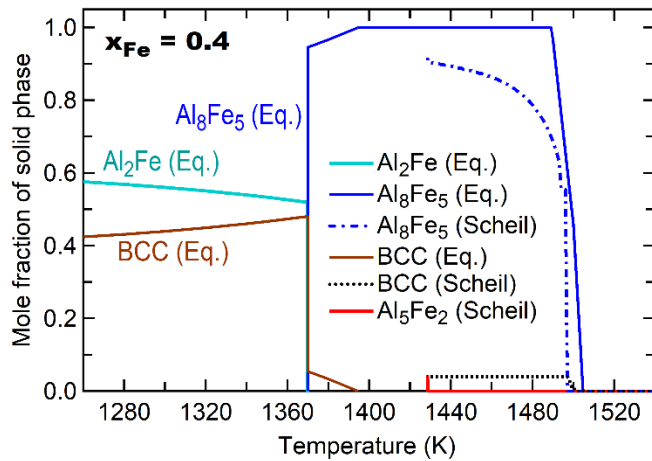


Figure 11. Calculated mole fractions of solid phases with $x_{\text{Fe}} = 0.4$ based on Scheil simulations and equilibrium (Eq.) calculations using the modelled data by Sundman et al.⁹.

Table 1. Experimentally observed Al-Fe IMCs in various processes in the literature. Note that the compositions quoted in this table are in wt.% unless otherwise stated.

#, Ref.	Materials	Methods	Observed Al-Fe IMCs
1 ¹⁰	Sheet ingots of Al alloys: 1050, -1100, and -5005	Direct-chill casting	Al ₁₃ Fe ₄ with cooling rate < 3 K/s; Al ₆ Fe with cooling rate from 1-3 to 10-20 K/s; and Al _m Fe (4 ≤ m ≤ 4.4) with cooling rate > 20 K/s
2 ¹³	Al-5Mg-xFe-0.6Mn (x = 0.1 ~ 2 wt.%)	High pressure die casting at 720 °C	Al ₆ (Fe,Mn) and Al ₁₃ (Fe,Mn) ₄ ^a
3 ¹⁴	Al-3Fe alloy	Equal channel angular extrusion at room temperature	Al ₆ Fe
4 ¹⁵	Al alloy 5A06 and SUS321 steel sheets	Tungsten inert gas welding-brazing with Al filler	Al ₆ Fe in welded seam with Nocokol flux; and Al ₁₃ Fe ₄ in the IMC layer
5 ¹⁶	Al-2.5wt.% Fe alloy powders	Laser powder bed fusion (LPBF)	Al ₁₃ Fe ₄ (reduced in the LPBF samples compared to ingots) and Al ₆ Fe
6 ¹⁷	Al and Fe powders	Layer by layer laser cladding	Al ₂ Fe (with 34 ~ 52 at. % Al cases); and Al ₅ Fe ₂ and Al ₁₃ Fe ₄ (with > 52 at. % Al cases)
7 ¹⁸	Al and Fe powders	Direct energy deposition (DED) type process	AlFe ₃ (for composition Fe-28Al); AlFe ₃ + AlFe (for Fe-36Al); and AlFe (for Fe-50Al)
8 ¹⁹	Fe-28Al and Al powders	Laser metal deposition for graded Fe-Al/steel samples and heat treated at 700 °C	AlFe and Al ₂ Fe (cracks originated in Al-rich part) followed by Al-rich AlFe below
9 ²⁰	Al and Fe wires	Wire-arc AM (WAAM) for Fe-AlFe functionally graded material (FGM)	AlFe ₃ and AlFe
10 ²¹	Al and Fe wires	WAAM to fabricate Fe-rich IMC (25 at.% Al)	AlFe ₃
11 ²²	Pure Al with Al-10 wt.% Fe	Vacuum centrifugal method to make Al-Al ₁₃ Fe ₄ FGM	Al ₁₃ Fe ₄
12 ⁴³	Compressed mixture of Al and Fe powders	High-temperature reactive sintering (800 and 900 °C)	Al ₅ Fe ₂ and Al ₂ Fe; and AlFe (long-term annealing)
13 ²³	Al-steel overlap joints	Laser welding (up to 1200°C)	Al ₅ Fe ₂ (assuming diffusion from Fe to Al only)
14 ²⁴	Al alloy 6061-T6 and galvanized steel DP590	Laser welding without filler	Al ₁₃ Fe ₄ and Al ₅ Fe ₂ with linear energy density of 162 J/mm; Al ₁₃ Fe ₄ , Al ₅ Fe ₂ , and AlFe with 309 J/mm
15 ²⁵	Al alloy 5083 and low alloy steel (XF350) plates	Fiber laser welding with 8 kW of max power	Al ₅ Fe ₂ near steel (main) and Al ₁₃ Fe ₄ near Al
16 ²⁶	Pure Al (1100) and low carbon steel	Friction stir welding	Al ₅ Fe ₂ and Al ₁₃ Fe ₄
17 ²⁷	Al alloy (5186) and low carbon steel	Friction stir welding	Al ₅ Fe ₂ (adjacent to Fe) and Al ₁₃ Fe ₄ (adjacent to Al, facilitated by Fe diffusion)
18 ²⁸	Al sheet (6061) and galvanized steel sheet	Friction stir welding	Al ₁₃ Fe ₄ (large size, diffusion induced) and AlFe ₃ (small size)
19 ²⁹	Al alloy 5754 with coated DP600 or 22MnB5 steel	Diffusion bonding by friction stir welding	Al ₅ Fe ₂ in low welding speeds (16 mm/min) and AlFe in 45 mm/min
20 ³⁰	Al alloy 5083 and steel (< 0.1 wt.% C) sheets	Annealing of friction stir lap welds	Al ₅ Fe ₂ (major) and Al ₁₃ Fe ₄ annealed at 673 K for 180 min
21 ³¹	Al alloy 6061-T6 and AISI 1018 steel	Friction welding	Al ₅ Fe ₂ and AlFe (suggested based on compositions)
22 ³²	Al sheet (6016) and galvanized IF-steel sheet	Friction stir spot welding	Al ₁₃ Fe ₄ , Al ₅ Fe ₂ , and Al ₂ Fe
23 ³³	Al alloy (surfalex 6 s) and ultrahigh strength steel	Friction stir scribe welding	Al ₅ Fe ₂ (in the middle) or Al ₁₃ Fe ₄ with Fe/Al solid solution depending on the weld regions
24 ³⁴	Al alloy (1050) sheets and Fe particles	Friction stir processing	Al ₅ Fe ₂ close to Fe particle; and Al ₁₃ Fe ₄ close to Al matrix
25 ³⁵	Al sheet (6061 T4) and coated steel sheet	Cold metal transfer fusion welding	Al ₁₃ Fe ₄ (at the interface to Al) and Al ₅ Fe ₂ (tongue-like, extended into steel)

26 ³⁶	Al alloy wire (ER5356) and Zn-coated steel	Double electrode gas metal arc welding	Al ₅ Fe ₂ (major) and Al ₁₃ Fe ₄
27 ³⁷	Pure Al and Fe	Solid Fe in liquid Al at 850 °C for 0.6 h	Al ₅ Fe ₂ layer with needle-like or flake Al ₁₃ Fe ₄
28 ³⁸	Pure Al and Fe	Immersion tests of solid Fe and liquid Al (700 ~ 900 °C)	Al ₅ Fe ₂ (adjacent to Fe) and Al ₁₃ Fe ₄ (adjacent to Al)
29 ³⁹	Pure Al and Fe	Immersion tests of solid Fe and liquid Al (700 ~ 900 °C)	Al ₅ Fe ₂ and Al ₁₃ Fe ₄
30 ⁴⁰	Pure Al plate and pure Fe sheet	Diffusion couples	Al ₅ Fe ₂ (at 873 K for 9 h) and Al ₁₃ Fe ₄ (at 913 K for 528 h)
31 ⁴¹	Pure Al and Fe rods (diffusion couples)	Al and Fe by isothermal bonding and then annealed at 973-1073 K	Al ₅ Fe ₂ (major, tongue-like) close to Fe and Al ₁₃ Fe ₄ close to Al
32 ⁴²	Al-Fe diffusion couples	Riveting Al rod into Fe plate	Al ₁₃ Fe ₄ formed in Fe side at 600 °C (Al diffuses to Fe) and Al ₅ Fe ₂ formed in both Al and Fe sides > 700 °C (due to Fe and Al interdiffusion)
33 ⁴⁴	Hot-dip Al-coated steel	Aluminized steel at 800°C for 60 s, then 680°C for 60 s	Al ₁₃ Fe ₄ just beneath Al cover layer and Al ₅ Fe ₂ just underneath steel

^a Addition of Mn promotes the formation of Al₆(Fe,Mn).

Table 2. Summary of phase stability of key Al-Fe IMCs with respect to pressure (P) and temperature (T) shown in **Figure 1**, **Figure 3**, and **Figure 6** (or not shown); together with their ductility/brittleness according to Pugh's criterion ^{11,12} as shown in **Figure 2**.

Al-Fe IMCs ^a	Ductility	P -favored?	T -favored?
Al ₆ Fe	Ductile	Yes	Not, or less effect
Al ₁₃ Fe ₄ (θ , Al ₃ Fe ⁹)	Slightly brittle	Always on convex hull ^b	Always on convex hull ^b
Al ₅ Fe ₂ (η , Al ₈ Fe ₃ ⁹³)	Brittle	Not, or less effect	Yes
Al ₂ Fe (MoSi ₂ -type)	Brittle	Yes, and strong	Not
Al ₈ Fe ₅ (D8 ₂ , ϵ ⁹)	Ductile	Less effect	Less effect
AlFe (B ₂)	Slightly brittle	Always on convex hull ^b	Always on convex hull ^b
AlFe ₃ (D0 ₃)	Ductile	Yes	Yes

^a Names used in the present work together with the names in the parentheses used in the literature.

^b These IMCs are always stable and on the convex hull in the present P and T of studied.

Supplementary Files

This is a list of supplementary files associated with this preprint. Click to download.

- [ShunliAlFeIMCsSlonlyv6.docx](#)